Demonstration of room temperature rectification in tapered-channel thermal diodes through confinement-induced liquid-solid phase change

Matt Jacobs,[1] Xinran Zhou,[2] Shu Huang,[2] Michal Marszewski,[3] Sarah Tolbert,[4] Stanley Osher,[1] Laurent Pilon,[3] and Jaime Marian[2,3,*]

[1] *Department of Mathematics, University of California Los Angeles, Los Angeles 90095, USA*
[2] *Department of Materials Science and Engineering, University of California Los Angeles, Los Angeles 90095, USA*
[3] *Department of Mechanical and Aerospace Engineering, University of California Los Angeles, Los Angeles 90095, USA*
[4] *Department of Chemistry and Biochemistry, University of California Los Angeles, Los Angeles 90095, USA*

(Dated: September 14, 2020)

Designing thermal diodes is attracting a considerable amount of interest in recent times due to the wide range of applications and potentially high impact in the transportation and energy industries. Advances in nanoscale synthesis and characterization are opening new avenues for design using atomic-level physics to take advantage of materials properties in confined volumes. In this paper we demonstrate using advanced modeling and simulation the rectification properties of tapered-channel thermal diodes relying on asymmetric heat flow brought about by thermal conductivity differences between the liquid and solid phases of suitably selected phase-change materials (PCM). Our prototypical design considers Ga as PCM and anodized alumina as structural material. First ,we carry out finite element simulations to study the effect of several geometric parameters on diode efficiency, such as channel length as aspect ratio. We then use a thresholding scheme to solve a Stefan problem in the device channel to study at the hysteresis of the phase transformation when the temperature gradient is switched. Our analysis establishes physical limits on rectification efficiencies and point to design improvements using complex materials to assess the potential of these devices as viable thermal diodes.

I. INTRODUCTION

A. Background

While electrical resistors and capacitors have thermal analogs in the form of linear static and passive thermal materials, no such analog exists for diodes and transistors (asymmetric heat flow and heat flow on demand). Such thermal devices would enable precise control of thermal energy transport and would significantly increase the efficiency and compactness of energy conversion and storage systems, heating and refrigeration, and thermal management of electronic devices and spacecrafts. Figure 1 schematically illustrates the transfer function of (a) a thermal diode and (b) a thermal switch, comparing them to a passive resistor of thickness L and thermal conductivity k [1]. Although the field is attracting significant research [1–3], discovering new materials with switchable and nonlinear thermal behavior relating to heat flow (analogous to electric current), or to temperature difference or thermal bias (analogous to voltage differential) still remains elusive due to a number of unresolved challenges. The principal difficulty is how to use standard thermal transport to achieve nonlinear phenomena such as thermal *rectification* (i.e., net directional heat flow). While a number of solutions have been proposed, producing rectification coefficients of sufficient magnitude over a wide temperature window has proven to be difficult [4, 5].

One potential pathway to induce asymmetric heat flow is to take advantage of the thermal conductivity differential between the liquid and solid phases of a given substance [3, 6]. Ideally, materials with fast, reversible, solid-liquid transitions must be used in conjunction with devices that control the phase transition based on the direction of heat flow. As recent research suggests, this can be achieved via nanoscale functional design [7, 8]. The central idea behind these devices is to take advantage of capillary *freezing point depression* of the phase-change material, i.e. achieving the phase transformation at different temperatures depending on whether it initiates from the liquid phase or from the solid phase. This can be achieved by designing a nanoporous material with parallel conical pores that result in a channel radius gradient across the device. The general design is illustrated in Figure 2, where conical channels with variable radius r are infiltrated with a phase-change material (PCM) that coexists in its solid and liquid forms thanks to freezing point depression. The two phases are separated by a curved moving interface that responds to changes in the thermal gradient, $\Delta T = T_h - T_c$. Depending on how this interface evolves, which determines the volume fraction of the liquid (poor thermal diffusivity) vs. the solid (good thermal diffusivity) phases, asymmetric heat flow can be induced.

* jmarian@ucla.edu; https://jmarian.bol.ucla.edu

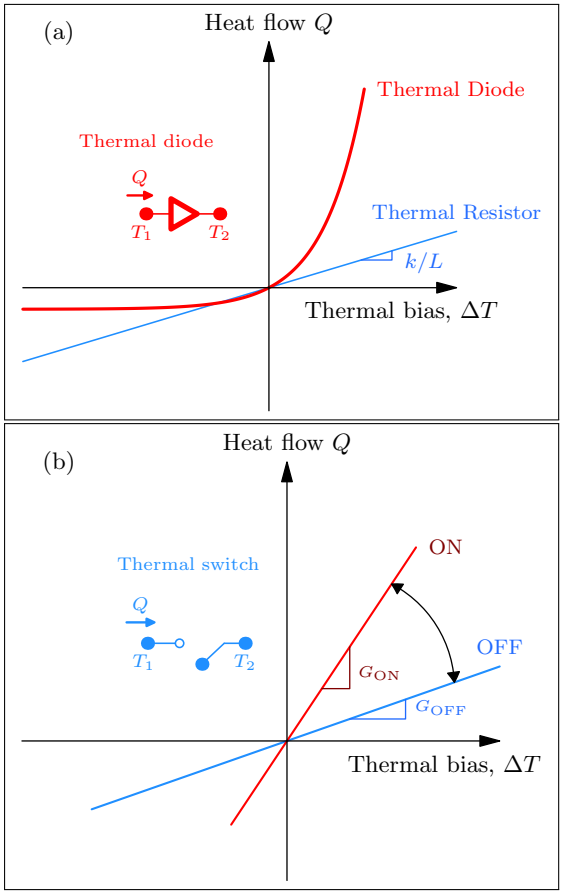

FIG. 1. Illustration of the transfer function of (a) thermal diodes and thermal resistors and (b) thermal switch that could be enabled thanks to asymmetric and nonlinear thermal behavior of novel materials (adapted from ref. [1]).

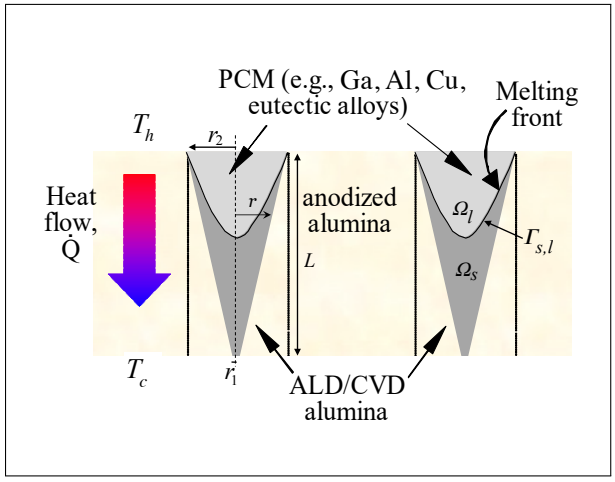

FIG. 2. Schematic diagram of the proposed thermal diode design. Conical channels with variable radius r are infiltrated with a phase-change material that coexists in its solid and liquid forms thanks to freezing point depression. The two phases are separated by a curved moving interface that responds to changes in the thermal gradient, $\Delta T = T_h - T_c$, giving rise to asymmetric heat flow.

B. Demonstration of concept viability via theory and modeling

Phase change materials undergoing rapid phase switching in nano confinement conditions are exceedingly difficult to study experimentally. In this context of extremely fine length and time scales, theory, modeling, and simulation are crucial tools to perform *a priori* analyses of the thermal diode's performance and physical viability. Of special interest is the motion along the channel of the liquid/solid interface in response to the thermal gradient, as its position determines the volume fraction of each phase and –consequently– the efficacy of the thermal conductivity differential.

This interface moves along either direction of the tapered channels depending on the sign of the temperature gradient, driven by both the free energy differential between the different phases and by curvature. Curvature is introduced both via the container design (channel walls) and from the liquid-solid interface. This can be modeled by solving a Stefan problem using fast and accurate algorithms for solving singular energy minimization problems. The objective of these simulations is to predict the solidification/melting dynamics of the system, including time response of the phase transition as a function of the material type and thermal gradient amplitude, crystallization microstructure, and possible hysteresis effects due to confinement and nucleation at the channel boundaries. The goal of the modeling effort is to simulate the cyclic response of these devices to variable switching of thermal gradients, as well as to identify suitable material candidates on the basis of their dynamic phase change properties.

Next, we provide a detailed description of the theory behind the models proposed, as well as a quantitative analysis and examples of different candidate materials based on their physical properties.

II. THEORY AND MODELING

A. Stefan Problem with surface tension

The standard formulation of the Stefan problem with surface tension (see for example refs. [9–12]) assumes the existence of a region Ω separated into a solid phase occupying a subregion Ω_s and a liquid phase occupying a subregion Ω_ℓ. Ω_s and Ω_ℓ are separated by an interface $\Gamma_{s,\ell}$ (cf. Fig. 2). Ω is bounded by an external interface Γ. The evolution of the temperature field in $\Omega \equiv \Omega_s + \Omega_\ell$ is

governed by:

$$\frac{\partial T}{\partial t} = \alpha_s \Delta T, \quad in\ \Omega_s \tag{1}$$

$$\frac{\partial T}{\partial t} = \alpha_\ell \Delta T, \quad in\ \Omega_\ell \tag{2}$$

$$T = T_m^* \left(1 - \frac{2\sigma_{s,\ell}}{\Delta h_f}\kappa\right), \quad on\ \Gamma_{s,\ell} \tag{3}$$

$$\frac{\partial \Gamma_{s,\ell}}{\partial t} = \Delta h_f^{-1} \left(\alpha_s \frac{\partial T}{\partial n_s} - \alpha_\ell \frac{\partial T}{\partial n_\ell}\right) \tag{4}$$

where α_s, α_ℓ are the heat diffusivity constants of the solid and liquid phase, Δh_f is the specific latent heat of fusion, T_m^* is the melting temperature, n is the unit normal to Γ pointing away from Ω_s and n_s and n_ℓ denote that the limit is taken either on the solid or liquid side. $\kappa = \kappa(x)$ is the mean curvature of $\Gamma_{s,\ell}$ at a point $x \in \Gamma_{s,\ell}$ with the convention that $\kappa \geq 0$ if the solid region is convex. The temperature condition on the interface is the classic Gibbs-Thompson law [13, 14], with $\sigma_{s,\ell} > 0$ the surface tension of the solid/liquid interface.

The above model can be augmented by assuming that the solid and liquid phases have surface energy interactions with the container wall. It can be then shown [15] that the surface tension must satisfy the triangle inequalities

$$\sigma_{s,w} \leq \sigma_{\ell,w} + \sigma_{s,\ell} \tag{5}$$

and

$$\sigma_{\ell,w} \leq \sigma_{s,w} + \sigma_{s,\ell}. \tag{6}$$

where $\sigma_{s,w}, \sigma_{\ell,w}$ are the surface tension at the interfaces between the wall and the solid and liquid, respectively, and $\Gamma_{s,w}, \Gamma_{\ell,w}$ are the interfaces between the wall and the solid and liquids respectively. Failure to satisfy these inequalities gives rise to the possibility of nucleation of one phase within the other. By way of example, if inequality (5) is not satisfied, it is energetically favorable for an arbitrarily thin region of liquid phase to nucleate between any contact surface of the solid and the wall.

In addition, at the point where the two phases and the wall meet, the system of equations (1)-(4) must be complemented with the so called *Herring* angle condition [16]:

$$\theta = \frac{\pi}{2}\left(1 + \frac{\sigma_{s,w} - \sigma_{\ell,w}}{\sigma_{s,\ell}}\right) \tag{7}$$

where θ is the opening angle of the intersection of the solid-wall and solid-liquid interfaces measured from inside the solid phase. Note that the triangle inequalities for the different surface tensions ensure that the angle is always between 0 and π.

B. Particularities of conically tapered channels

The system of eqs. (4) to (7) is now solved in a tapered conical channel of the type shown schematically in Fig. 2. Assuming that the interface equilibrates to constant curvature, one can derive from eqs. (3) and (7) an expression for the so-called *freezing point depression*, i.e., a size dependent T_m^*:

$$T_m^*(r) = T_m^0 \left(1 - \frac{2\sigma_{s/\ell,w}}{r\Delta h_f}\right) \quad \text{on } \Gamma \tag{8}$$

where T_m^0 is the bulk melting temperature, $\sigma_{s/\ell,w}$ is a coefficient that accounts for the relative affinity of the solid 's' and liquid 'ℓ' phases for the container wall, and where it has been assumed that $\kappa \propto r^{-1}$ is the curvature of any annular section of constant radius r of the cone. As explained in Sec. I A, the efficacy of our thermal diode design is predicated on the ratio k_ℓ/k_s. Note that, for clarity, in this section we work with the thermal conductivities $k_{\ell,s} = \alpha\rho C_p\big|_{\ell,s}$, where ρ and C_p are the mass density and the heat capacity of the corresponding liquid or solid phase. Table I lists a number of candidate PCMs with their corresponding bulk melting temperatures and ordered by increasing thermal conductivity ratio. As the data in the table reveal, some PCMs display significant thermal conductivity decreases upon melting. More importantly, the thermal conductivity differential is highest for the pure metals Al, Cu, Sn, and Ga. However, substances whose solid/liquid transition occurs near room temperature are of particular interest in this work, as they offer a potentially wider range of applicability. Of those shown in the table, Ga is the option with the best combination of melting temperature and low k_ℓ/k_s ratio. Figure 3 shows measurements of k_s and k_ℓ for commercial Ga [18, 19], showing the gap between the solid and liquid phases. The behavior for the other pure metals is found to be qualitatively very similar.

TABLE I. List of candidate PCMs with their corresponding bulk melting temperatures, ordered by their thermal conductivity ratio. Temperatures are in degrees Celsius and thermal conductivities in $\mathrm{W{\cdot}m^{-1}{\cdot}K^{-1}}$ (from various sources. [17]).

PCM	T_m^0	k_s	k_ℓ	k_ℓ/k_s
Al	657	218	94	0.43
Cu	1090	339	166	0.49
Sn	220	60	30	0.49
Ga	30	42	25	0.59
$Bi_{50}Pb_{27}Sn_{13}Cd_{10}$	70	33	22	0.68
CdZn	266	86	60	0.70
$Sn_{60}Bi_{40}$	200	27	19	0.70
SnCu	227	59	45	0.76
ZnMg	366	137	107	0.78
SnPb	183	40	32	0.80

Taking advantage of the k_ℓ/k_s ratio is also important for our design to find materials with the highest melting point differential $\Delta T^{\mathrm{fr}} = T_m^*(r) - T_m^0$. One can obtain estimates for ΔT^{fr} directly from eq. (8) using the parameters of Table II:

$$\Delta T^{\mathrm{fr}} = \frac{2T_m^0 \sigma_{s,\ell} \cos\theta}{r\rho_s \Delta h_f} \tag{9}$$

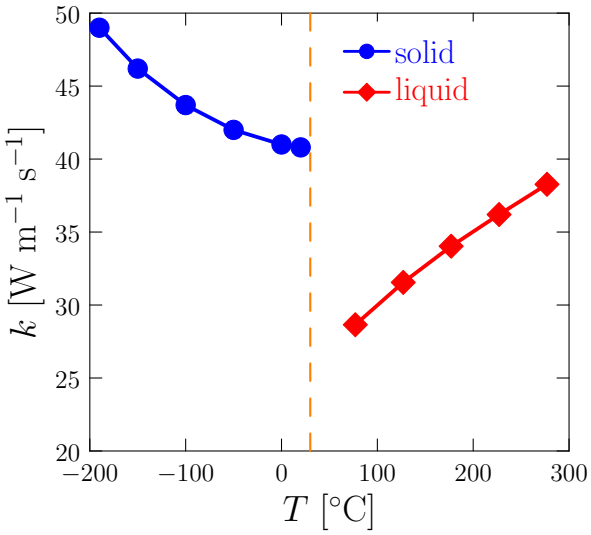

FIG. 3. Evolution of the thermal conductivity of pure Ga as a function of temperature. The dashed line marks the melting point, at which a noticeable drop is observed [18, 19].

where ρ_s is the density of the solid phase. For the moment, we assume that $\sigma_{w,s/\ell} = \sigma_{s,\ell}\cos\theta$ (recall that θ here is the angle from the Herring angle condition (7)).

Published values for the rest of the parameters in eq. (9) are given in Table II. From those, we get the dependence of the freezing point depression with section radius shown in Figure 4 as given by:

TABLE II. Values for the parameters used in eqs.(4) and (9) for Ga (from refs. [20–22]). Note that, for the different surface tensions given, the Herring angle is 27.5° according to eq. (7).

constant	units	value
T_m^0	K	302.8
$\sigma_{s,\ell}$	J m^{-2}	0.056
$\sigma_{s,w}$	J m^{-2}	1.63
$\sigma_{\ell,w}$	J m^{-2}	1.80
θ	deg	30
ρ	g m^{-3}	5.91×10^6
Δh_f	J g^{-1}	80.4

$$\Delta T^{\mathrm{fr}} = 6.16 \times 10^{-8} r^{-1}$$

with ΔT^{fr} in K when r is in m. The graph suggests that channels with cross sections smaller than 5-nm in radius are needed to take advantage of freezing point depression (12.5 K at $r = 5$ nm).

C. Numerical approach

Our numerical approach to solving eqs. (4) is based on an iterative energy minimization scheme of a nonlocal surface energy functional $\mathcal{H}_\epsilon$. To that end, let now Ω_s, Ω_ℓ, and Ω_w specifically denote the volume fractions of the solid, liquid, and outer wall regions (see Fig. 2):

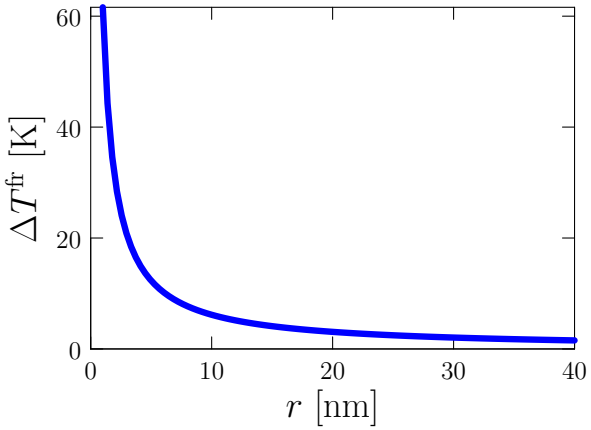

FIG. 4. Freezing point depression in Ga as a function of the radius of curvature.

$$\mathcal{H}_\epsilon(\Omega_s, \Omega_\ell, \Omega_w) = \frac{1}{\sqrt{\epsilon}}\left[\sigma_{s,\ell}\int_\Omega \Omega_\ell(x)(H_\epsilon * \Omega_s)(x)\,dx + \int_\Omega (\sigma_{s,w}\Omega_s(x) + \sigma_{\ell,w}\Omega_\ell(x))(H_\epsilon * \Omega_w)(x)\,dx\right] \quad (10)$$

where H_ϵ is a heat kernel [23] that is convolved in space with each of the Ω_α at time $t = \epsilon$. Integration in the above equations is understood to occur over the entire configurational volume (dx is shorthand notation for an infinitesimal volume element). When ϵ tends to zero, the heat content energy converges to the usual surface tension energy [24]. Note that the outer pore walls are fixed, hence Ω_w cannot change over time. Furthermore, in the pore interior, we must have the relation $\Omega_s + \Omega_\ell = 1$. Thus, we only need to keep track of the relative concentration of the solid phase. Thus we write $\Omega = \Omega_s$ and view the functional $\mathcal{H}_\varepsilon$ as a function of Ω only.

The solver employed to minimize the above functional is based on a *thresholding* scheme, the likes of which have proven to be robust methods for dealing with sharp interfaces [24–26]. At a step i with known temperature and concentration of the solid phase (T^i and Ω^i, respectively), we obtain T^{i+1} and Ω^{i+1} via the following three steps:

$$T^{i+\frac{1}{2}} - T^i = \tau\nabla\cdot\left(\left[\alpha_s\Omega^i + \alpha_\ell(1-\Omega^i)\right]\nabla T^{i+\frac{1}{2}}\right) \quad (11)$$

$$\Omega^{i+1} = \mathrm{Thresh}\left(\Omega^i + \frac{T_m\exp\left(-\frac{1}{\Delta h_f}\mathcal{H}_\epsilon(\Omega^n)\right) - T^{i+\frac{1}{2}}}{\Delta h_f}\right) \quad (12)$$

$$T^{i+1} = T^{i+\frac{1}{2}} + \Delta h_f(\Omega^{i+1} - \Omega^i) \quad (13)$$

As in Sec. II A, α_s and α_ℓ are the heat diffusivities of the solid and liquid phases, Δh_f is the latent heat of fusion,

τ is the time step, and for any real-valued number a:

$$\text{Thresh}(a) = \begin{cases} 0 & \text{if } a < 0, \\ a & \text{if } a \in [0,1], \\ 1 & \text{if } a > 1. \end{cases}$$

Equation (11) is an approximation to the evolution of the heat equation for time τ. Note that equation (11) takes into account the difference in thermal conductivity between the solid and liquid phases. The expression for the second step, eq. (12), comes from the solution of a variational problem that ensures that the scheme above is unconditionally stable. Roughly, eq. (12) balances the competing effects of surface tension and melting temperature on the relative concentrations of the solid and liquid phases. The final step, eq. (13), updates the temperature by taking into account the heat that is released (absorbed) by freezing (melting).

One of the advantages of this approach is that the Gibbs-Thompson condition [given in eq. 4] at the interface is encoded in the update steps (12) and (13), without needing to be explicitly defined.

III. RESULTS

Next we present results for the Ga-Al_2O_3 tapered channel design described above.

A. Rectification and optimum thermal diode design

The initial geometry of the thermal diode building block structure can be optimized to maximize the rectification, i.e., the ratio of heat fluxes in the forward and reverse directions for given thermal conductivities of the substrate solid and liquid phases, and melting temperature of the PCM filling the conical channel. This rectification can be obtained by solving the system of equations (1)-(4) in geometries such as that provided in Fig. 2 subjected to a prescribed temperature gradient. The goal in this section is to optimize the aspect ratio of the tapered channels [28] for a fixed channel length to maximize rectification and guide synthesis processes.

To that end, we use the finite element code `Abaqus` in geometries defined by a total channel length $L = 400$ nm, and a radius at the narrow end of the conical section of $r_2 = 5$ nm. The wide-end radius is left as an outcome of the maximization exercise, but we set its minimum value to $r_1 = 40$ nm. The temperature window is always centered at T_m^0, and we use a thermal conductivity for anodized alumina of 1.0 $\text{W}\cdot\text{m}^{-1}\cdot\text{K}^{-1}$ [29]. Figure 5 shows the rectification behavior for the Ga-Al_2O_3 tapered channel design with $r_2/r_1 = 40/5$, with the shaded areas in each quadrant of the graph giving the range of attainable rectifications. The dotted lines mark the ideal rectification as set by a full solid phase (forward thermal gradient) or a full liquid phase (reverse gradient) of the PCM in the channel. Figure 6 shows color maps of the steady-state temperature and heat flux fields for the same design as in Fig. 5 when in the reverse configuration (heat flowing towards the left).

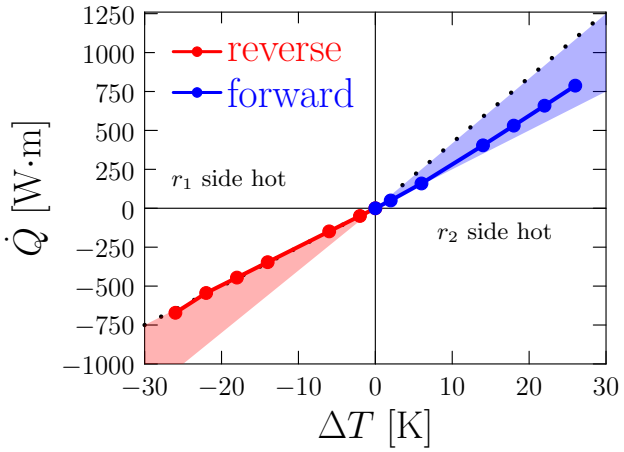

FIG. 5. `Abaqus` (finite element) calculations of the rectification effect for the the Ga-Al_2O_3 tapered channel design with $r_2/r_1 = 40/5$ proposed in this work. The shaded areas in each quadrant of the graph give the range of attainable rectifications. The dotted lines mark ideal rectification as set by a full solid phase (forward thermal gradient) or a full liquid phase (reverse gradient). The heat flux is multiplied times the length of the tapered channel (400 nm) and thus given in W·m.

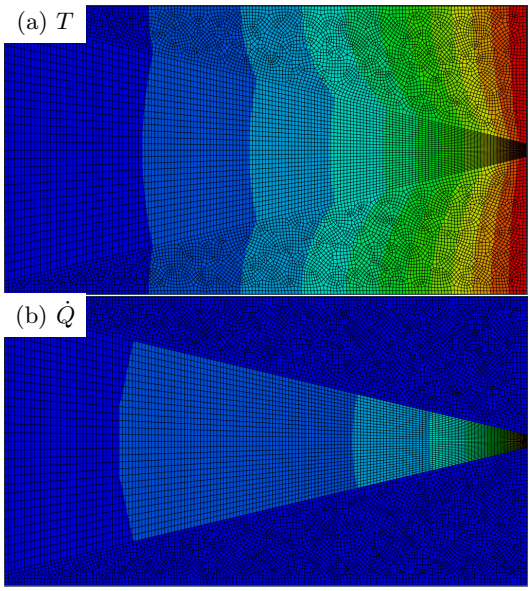

FIG. 6. Color maps in arbitrary units of the steady state `Abaqus` solutions for the 40/5 diode ($L = 400$ nm). (a) Temperature field. (b) Heat flux. Both images are for forward conduction.

The data in Fig. 5 were used to calculate the rectification R of the device, obtained using a widely-accepted

definition for R [1, 30, 31]:

$$R = \frac{\dot{Q}_f}{\dot{Q}_r} - 1 \tag{14}$$

The results are shown in Figure 7, where a gradual increase in R is seen up to $\Delta T = 22$ K when the maximum value of 21 % is reached. While these are the actual values for the specific design proposed here, note that the maximum (theoretical) rectifications attainable are those corresponding to heat fluxes on the boundaries of the shaded regions in Fig. 5 (marked by dotted lines), corresponding to $R = 68$ %. Consequently, one can propose

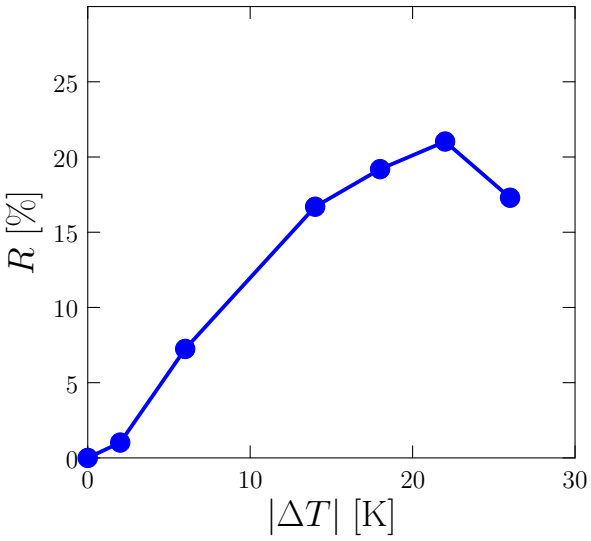

FIG. 7. Device rectification calculated with eq. (14) using the data in Fig. 5.

a rectification *efficiency*, based on the relative 'distance' of the simulated curve to the ideal limits [3]:

$$\eta = \sum_i^N \left(1 - \frac{\left| \dot{Q}_s^{\rm sim} - \dot{Q}_{s,\ell}^{\rm id} \right|}{\left| \dot{Q}_s^{\rm id} - \dot{Q}_\ell^{\rm id} \right|} \right) \tag{15}$$

where N is the total number of data points, and $\dot{Q}^{\rm id}$ and $\dot{Q}^{\rm sim}$ are the ideal and simulated heat fluxes for a given ΔT. With this definition, points lying on the dotted lines in Fig. 5 would give an efficiency of 100%. The efficiencies are averaged across all ΔT-points for each branch, so that we have distinct forward and reverse efficiencies. For the design considered here, $\eta \approx 99\%$ for the reverse configuration (all liquid) and $\approx 21\%$ for the forward direction (partially liquid and solid).

Next, we carry out several simulations varying r_1 and L to calculate the associated efficiencies as optimization estimators. The results for both conducting branches are given in Table III. The rectification efficiency is practically independent of the total length L of the thermal diode. Similarly, $\eta_{\rm f}$ appears to be quite insensitive to the value of r_1 above approximately 40 nm. Figure 8 shows the evolution of the $\eta_{\rm f}$-r_1 relationship for r_1 in the 20-to-400-nm interval.

TABLE III. Rectification efficiency as determined using eq. (15) for the 'forward' and 'reverse' branches of the thermal diode design as a function of the large end radius r_1 and total length L of the conical channel. r_2 is fixed at 5 nm here.

$L = 400$ nm			
r_1 [nm]	20	40	60
$\eta_{\rm f}$ [%]	15	21	26
$\eta_{\rm r}$ [%]	100	99	98
$r_1 = 40$ nm			
L [nm]	100	200	400
$\eta_{\rm f}$ [%]	22	21	21
$\eta_{\rm r}$ [%]	99	99	99

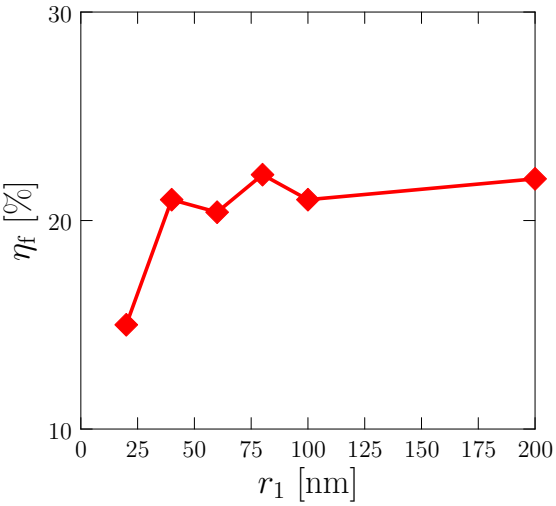

FIG. 8. Rectification efficiency along the conducting ('forward') direction of the thermal diode design proposed in this work as a function of the large conical radius r_1. All data points are for fixed values of $r_2 = 5$ nm and L =400 nm.

These findings point towards designs with aspect ratios r_1/r_2 larger than 40/5. However, as long as that condition is satisfied, the large radius of the tapered conical channel can be flexibly selected on the basis of device synthesis considerations.

B. Modeling solid/liquid interface effects and thermal gradient hysteresis

While the above results are useful to gain insight into the global behavior of the thermal diode design, they ignore critical physical processes that take place at the solid/liquid interface. For example, the finite element calculations assume a flat solid/liquid interface that responds symmetrically to switching the thermal gradient. However, it is known that contact effects and surface tension break the directional symmetry of the interface with

respect to the direction of heat flow. In this section we study the physical behavior of the s/ℓ interface solving the Stefan problem defined in eqs. (4) explicitly by following the numerical procedure described in Section II C. We restrict our study to the thermal diode design with $L = 400$ nm and $r_1/r_2 = 40/5$.

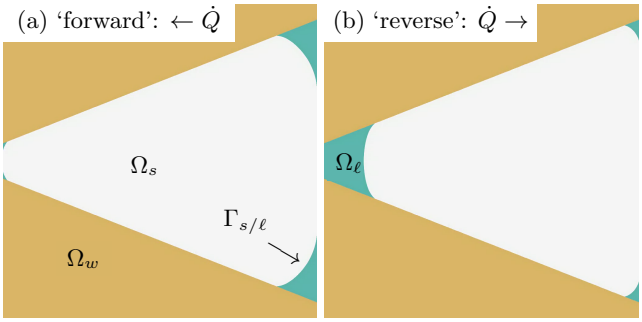

FIG. 9. Stationary state of a Stefan problem with fixed temperature values on the boundary. The white, blue and brown regions represent the solid, liquid and pore walls respectively. (a) The temperature on the left-hand side boundary of the pore is lower than the temperature on the right-hand side boundary (260 vs. 340 K). The device is the 'forward' position, allowing heat to quickly flow from the right-hand side to the left. (b) The device is in the 'reverse' position, and heat is transferred more slowly from the left-hand side to the right compared to the situation in (a).

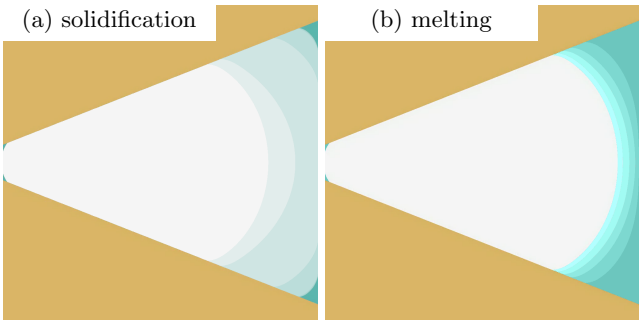

FIG. 10. (a) Solidification of the liquid phase when the temperature at the right-hand side boundary is fixed at 20 K below the melting point. The white region in the center is the part of the pore that is initially in the solid phase. The next lightest region solidifies in the first 5 seconds of the evolution, and so on. Steady state is reached after 15 seconds, when the solid fills all of the pore except for the darkest blue region. (b) Melting of the solid phase when the temperature at the right-hand side boundary is fixed at the melting point. Initially, the entire pore is solid. The darkest blue region melts in the first 5 seconds of the evolution. The next darkest region melts during in the next 5 s, etc. The white region in the center remains solid after 25 seconds have elapsed.

We begin by studying the steady state of a Stefan problem with fixed temperature values on the boundary. In the following figures, the white, blue and brown regions represent, respectively, the solid (Ω_s), liquid (Ω_ℓ), and pore walls (Ω_w). Figure 9 gives the converged solution for the 'forward' (heat flowing from right to left) and 'reverse' (left to right) cases. For Fig. 9(a), the temperature on the left boundary of the pore is lower than the temperature on the right (260 vs. 340 K). The temperatures on each side are sufficiently low to prevent complete melting of the solid phase. As a result the device is in the 'forward' position, allowing heat to quickly flow from the right to left. In Fig. 9(b), the temperature boundary condition is reversed with respect to 9(a). Due to the melting point depression effect, the solid completely melts in the narrow part of the pore on the left-hand side and, as a result, the device is in the 'reverse' position with heat being transferred from left to right more slowly than in the inverse situation. In both cases, notice how the relative balance of surface energies makes the interface curvature always concave with respect to the origin at the center of the narrow end of the channel.

Perhaps more interesting is to study the dynamic asymmetry between the melting and solidification processes when the temperature gradient is reversed. This is illustrated graphically in Figure 10, where the interface position is tracked as it evolves in response to thermal switching. In Fig. 10(a), solidification of the liquid phase is shown when the temperature at the right boundary is fixed at 20 K below T_m^0. The white region in the center is the part of the pore that is initially in the solid phase. The next lightest region solidifies in the first 5 seconds of the evolution and so on. The steady state is reached when the solid fills all of the pore except for the darkest blue region, after approximately 15 s. In Fig. 10(b), the temperature gradient is inverted and the melting front is tracked and plotted in five-second intervals. The white region in the center remains solid after 25 s, when steady state is reached. This clearly points to an asymmetry along the direction of propagation of the front, which can be appreciated in Figure 11. The figure shows a quasi-hysteresis cycle encompassing 25 seconds of forward thermal switching (inducing solidification) followed by an equal amount of time under the reverse gradient. As seen in the figure, at the end of the melting stage the front is found at some distance away from the base of the conical channel. The slopes of the blue and red branches give the velocities of propagation of the interface at each time.

Ideally, these results can be used to inform the finite-element calculations shown in Fig. 6 so as to create a self-consistent feedback loop that yields converged rectification factors when the shape and dynamics of the interface are taken into account. We consider such exercise to be beyond the present scope of this study (although we speculate that it may lead to slightly lower rectifications due to the convex shape of the interface).

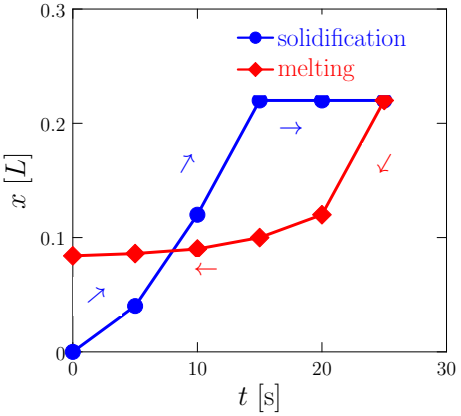

FIG. 11. Position of the center point (on long axis of the conical channel) in units of L of the solid/liquid interface as a function of time for a full thermal switching cycle. Time follows the direction of the arrows.

IV. DISCUSSION

A. Numerical demonstration of rectification and hysteresis

This work is essentially a numerical demonstration of net rectification in conical tapered channels containing a phase-change material enclosed in a nanoscale architecture made up of a thermal insulating material. On the basis of this design, we can act on different degrees of freedom to increase rectification:

1. On the materials side, the use of PCMs with the widest difference between the liquid and solid thermal conductivities yields the widest possible rectification range (see shaded regions in Fig. 5).

2. On the geometry side, the ideal design is that whose forward and reverse thermal biases can come closest to the pure liquid and solid limits. For this, the geometry that best takes advantage of the freezing point depression emanating from nano-confinement of the PCM in tapered channels is one with a high r_1-to-r_2 ratio.

While these considerations pertain to static properties of the device, dynamic effects must also be considered as part of the design/operation process. In particular, the nature of the s/ℓ interface and its propagation in the forward and reverse directions is seen to control the speed of the transformation and the capability to fully achieve the theoretical efficiency as presented in, e.g., Fig. 8. As demonstrated in Sec. III B, the surface tension between the solid, liquid, and channel wall materials controls the s/ℓ interface curvature, which in turn results in a propagation asymmetry between the forward and reverse thermal gradient directions. This asymmetry gives rise to a hysteresis cycle that must be carefully studied to avoid long-term detrimental effects associated with thermal and mechanical fatigue, which could eventually lead to device failure.

While the present design based on porous alumina infiltrated with metallic gallium is suitable for operation near room temperature, other concepts based on 3D nanoscale architectures for higher temperatures can also be considered. As Table I suggests, materials such as Al and Cu have the potential for higher rectification efficiencies when operated at higher temperatures, such that thermal diode designs where these materials act as the PCM may show promise for tapered conical geometries. Eutectic phases of the materials listed in Table I with melting temperature above 500°C and relatively high thermal conductivities (e.g., >20∼40 $\mathrm{W{\cdot}m^{-1}{\cdot}K^{-1}}$) may also be considered as alternate phase-change materials. High-temperature thermal diodes, however, may be susceptible to oxidation, which adds another dimension to the design space.

B. Potential pathways for material selection and synthesis

The initial synthesis and model materials envisioned could consist of synthesizing tapered pores by non-conformal deposition of an insulating material (such as alumina) using a combined atomic layer and chemical vapor deposition (ALD/CVD) method in anodic alumina membranes with cylindrical pores. Then, the tapered pores are infiltrated with eutectic liquid metal alloys such as those of gallium (Ga), indium (In), and tin (Sn). The degrees of freedom in the thermal diode synthesis would include:

(i) Porosity control via anodic etching conditions.

(ii) Control of porosity gradient via ALD/CVD.

(iii) Control of melting temperature (via eutectic composition and PCM nano confinement).

In addition, ALD/CVD can provide control of the thermal resistance between the low thermal conductivity alumina and the high thermal conductivity PCM.

Finally, other geometry concepts may be explored. For example, templated nanoporous silicon carbide (SiC) with spherical pores infiltrated with molten salts may constitute attractive alternatives to the conical channel designs explored in this paper.

V. CONCLUSIONS

Our main conclusions are listed below:

1. We have demonstrated the room temperature rectification of gallium-infiltrated Al_2O_3 tapered-channel thermal diodes through confinement-induced liquid-solid phase change.

2. The design relies on the onset of asymmetric heat flow due to a thermal conductivity differential (Fig. 3)between the solid and liquid phases of a suitable phase-change material that undergoes a phase transformation in the temperature range of operation of the thermal diode (Fig. 4).

3. Finite-element calculations indicate that, for the prototypical design with $L = 400$ nm, $r_1 = 40$ nm, and $r_2 = 5$ nm, a maximum rectification of 21 % is achieved (Fig. 7). The maximum theoretical rectification for this design is 68 %.

4. Above 25 nm, the value of r_1 has practically no effect on the thermal efficiency of the thermal diode.

5. Modeling of the solid/liquid interface and its interactions with the channel walls suggests convex shapes and a hysteretic dynamic cycle with equilibration times of 25 s (Figs. 9, 10, and 11). The models involve fast interface tracking algorithms using thresholding techniques to solve Stefan problems.

6. Our results can be used as a springboard to consider other PCM that can operate at elevated temperatures with higher rectifications.

ACKNOWLEDGMENTS

The authors acknowledge the support from UCLA's Office of the Vice Chancellor for Research under seed grant for developing interdisciplinary research groups.

[1] G. Wehmeyer, T. Yabuki, C. Monachon, J. Wu, and C. Dames, Thermal diodes, regulators, and switches: Physical mechanisms and potential applications, Applied Physics Reviews **4**, 041304 (2017).

[2] B. Li, L. Wang, and G. Casati, Thermal diode: Rectification of heat flux, Physical review letters **93**, 184301 (2004).

[3] P. Ben-Abdallah and S.-A. Biehs, Phase-change radiative thermal diode, Applied Physics Letters **103**, 191907 (2013).

[4] E. Pereira and R. R. Ávila, Increasing thermal rectification: Effects of long-range interactions, Physical Review E **88**, 032139 (2013).

[5] T. Hess, L. Maier, P. Corhan, O. Schäfer-Welsen, J. Wöllenstein, and K. Bartholomé, Modelling cascaded caloric refrigeration systems that are based on thermal diodes or switches, International Journal of Refrigeration **103**, 215 (2019).

[6] A. L. Cottrill and M. S. Strano, Analysis of thermal diodes enabled by junctions of phase change materials, Advanced Energy Materials **5**, 1500921 (2015).

[7] C. B. Sobhan and G. P. Peterson, *Microscale and nanoscale heat transfer: fundamentals and engineering applications* (CRC Press, 2008).

[8] T. Luo and G. Chen, Nanoscale heat transfer–from computation to experiment (2013).

[9] L. Caffarelli and L. Evans, Continuity of the temperature in the two-phase stefan problem, Archive for Rational Mechanics and Analysis **81**, 199 (1983).

[10] I. I. Danilyuk, On the stefan problem, Russian Mathematical Surveys **40**, 157 (1985).

[11] A. Visintin, Stefan problem with surface tension, in *Mathematical Models for Phase Change Problems* (Springer, 1989) pp. 191–213.

[12] A. M. Meirmanov, *The Stefan Problem*, Vol. 3 (Walter de Gruyter, 2011).

[13] Z. Liu, K. Muldrew, R. G. Wan, and J. A. W. Elliott, Measurement of freezing point depression of water in glass capillaries and the associated ice front shape, Phys. Rev. E **67**, 061602 (2003).

[14] F. Liu, L. Zargarzadeh, H.-J. Chung, and J. A. Elliott, Thermodynamic investigation of the effect of interface curvature on the solid–liquid equilibrium and eutectic point of binary mixtures, The Journal of Physical Chemistry B **121**, 9452 (2017).

[15] B. Widom, Interfacial tensions of three fluid phases in equilibrium, The Journal of Chemical Physics **62**, 1332 (1975).

[16] C. Herring, Some theorems on the free energies of crystal surfaces, Physical review **82**, 87 (1951).

[17] M. R. Landry, Thermoporometry by differential scanning calorimetry: experimental considerations and applications, Thermochimica acta **433**, 27 (2005).

[18] M. Duggin, The thermal conductivity of liquid gallium, Physics Letters A **29**, 470 (1969).

[19] R. Powell, M. J. Woodman, and R. Tye, Further measurements relating to the anisotropic thermal conductivity of gallium, British Journal of Applied Physics **14**, 432 (1963).

[20] D. Turnbull, Formation of crystal nuclei in liquid metals, Journal of Applied Physics **21**, 1022 (1950).

[21] D. P. Woodruff and D. P. Woodruff, *The solid-liquid interface* (CUP Archive, 1973).

[22] M. Losurdo, A. Suvorova, S. Rubanov, K. Hingerl, and A. S. Brown, Thermally stable coexistence of liquid and solid phases in gallium nanoparticles, Nature materials **15**, 995 (2016).

[23] Typically a Gaussian of the form: $H_\epsilon = (\epsilon)^{-2} \exp(-\pi|x|^2/\epsilon^2)$.

[24] S. Esedolu and F. Otto, Threshold dynamics for networks with arbitrary surface tensions, Communications on Pure and Applied Mathematics **68**, 808 (2015), https://onlinelibrary.wiley.com/doi/pdf/10.1002/cpa.21527.

[25] Gallouët, Thomas, Laborde, Maxime, and Monsaingeon, Léonard, An unbalanced optimal transport splitting scheme for general advection-reaction-diffusion problems, ESAIM: COCV **25**, 8 (2019).

[26] M. Jacobs and F. Léger, A fast approach to optimal transport: The back-and-forth method, arXiv preprint arXiv:1905.12154 (2019).

[27] F. Otto, The geometry of dissipative evolution equations: the porous medium equation, Comm. Partial Differential Equations **26**, 101 (2001).
[28] Defined here as the ratio of the radius of the wide section of the conical channel r_1 to the radius of the narrow section r_2, r_1/r_2.
[29] J. Lee, Y. Kim, U. Jung, and W.-S. Chung, Thermal conductivity of anodized aluminum oxide layer: The effect of electrolyte and temperature, Materials Chemistry and Physics **141**, 380 (2014).
[30] A. Ghanekar, J. Ji, and Y. Zheng, High-rectification near-field thermal diode using phase change periodic nanostructure, Applied Physics Letters **109**, 123106 (2016).
[31] B. Li, L. Wang, and G. Casati, Thermal diode: Rectification of heat flux, Phys. Rev. Lett. **93**, 184301 (2004).